# DSVO: Direct Stereo Visual Odometry

Jiawei Mo[1] and Junaed Sattar[2] *

November 25, 2021

## Abstract

This paper proposes a novel approach to stereo visual odometry without stereo matching. It is particularly robust in scenes of repetitive high-frequency textures. Referred to as DSVO (Direct Stereo Visual Odometry), it operates directly on pixel intensities, without any explicit feature matching, and is thus efficient and more accurate than the state-of-the-art stereo-matching-based methods. It applies a semi-direct monocular visual odometry running on one camera of the stereo pair, tracking the camera pose and mapping the environment simultaneously; the other camera is used to optimize the scale of monocular visual odometry. We evaluate DSVO in a number of challenging scenes to evaluate its performance and present comparisons with the state-of-the-art stereo visual odometry algorithms.

## 1 Introduction

It is an essential ability for an autonomous mobile robot to localize itself, especially in GPS-denied locations such as indoors and underwater. Stereo visual odometry has been widely used for robot localization, which estimates ego-motion using only a stereo camera. Visual sensors, and thus stereo cameras, are *passive* sensors which do not use emissions and thus consume less energy compared with *active* sensors such as laser range-finders (*i.e.*, LiDAR). Mobile robots, particularly those operating outdoors or in unstructured domains, benefit greatly from efficient energy usage as it extends the length of deployments, and also reduces downtime between missions.

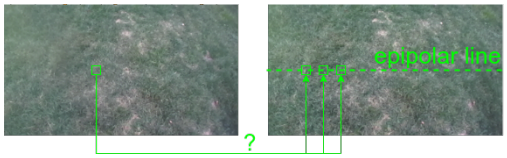


Figure 1: Stereo matching ambiguity in a scene of repetitive high-frequency textures (grass).

Most stereo visual odometry systems (*e.g.*, [9, 11, 18]) depend on stereo matching. Stereo matching algorithms can be categorized into local methods and global methods [7]. Local methods (*e.g.*, [1,3,4]) focus on small patches around the target feature. The correspondences are found by searching for the most similar patch along the epipolar line on the corresponding stereo frame. This strategy is computationally efficient and can perform in real-time. However, it is not robust, especially for repetitive high-frequency textures such as grass or sand. These scenes are not uncommon outdoors and are often encountered by field robots, such as underwater or mine-exploration robots. Even though the search space is constrained by the epipolar line, there could still be more than one similar patch that would give rise to ambiguity in best-match determination. Figure 1 shows an example to demonstrate this problem. To improve the robustness, global stereo matching methods exploit non-local constraints, such as smoothness, to reduce sensitivity to regions with challenging texture. However, their computational complexity is often quite high and additional hardware (such as GPUs) may be required for real-time performance. This adds to

*The authors are with the Department of Computer Science and Engineering, University of Minnesota Twin Cities, Minneapolis, MN, USA. {[1]moxxx066, [2]junaed} at umn.edu.

energy consumption and increases system complexity, which is not desirable for mobile robots.

On the other hand, SVO [12], a semi-direct monocular visual odometry, has demonstrated high-accuracy in scenes of repetitive high-frequency textures. It estimates an initial camera pose by minimizing photometric error directly. SVO then projects 3D map-points (landmarks) onto the current frame according to the initial camera pose. Subsequently, it searches feature correspondence for each map-point locally in a small area around the projection. The camera pose is further optimized by the feature correspondences. While SVO is quite accurate and efficient, the ego-motion estimated by SVO or any monocular visual odometry is not fully recovered. The camera translation and the reconstructed map-points are up to scale; even worse, the scale tends to drift. The unknown scale is not a problem for certain applications such as augmented reality, but knowing the scale is important for mobile robots. For example, the scale is crucial for robot control, and path planning.

To address the scale problem, authors of [5, 21, 28] fuse monocular visual odometry with an inertial measurement unit (IMU) to create a visual-inertial odometery (VIO). In this case, the IMU provides scale estimation for monocular visual odometry. However, IMU pose propagation is sensitive to measurement noise, and visual measurements are used to correct the propagated pose. VIO systems achieve high accuracy and efficiency with a reliable IMU, which needs to be initialized at the beginning.

In this work, we propose a novel approach to visual odometry which we call **D**irect **S**tereo **V**isual **O**dometry (DSVO). It solves the scale problem of monocular visual odometry by integrating an additional camera rather than an IMU. It combines the strengths of stereo and monocular visual odometry and is able to outperform each in terms of accuracy and performance. DSVO works by running a semi-direct monocular visual odometry on one camera of the stereo pair to track the ego-motion. To address the scale problem, we project the 3D map-points from the monocular visual odometry onto the other camera. The optimal scale is solved by minimizing the photometric error in stereo projection. The main contributions of this work are:

- A novel algorithm for stereo visual odometry without stereo matching or any explicit feature matching;
- Robustness for repetitive high-frequency textures;
- Full estimation of ego-motion with optimized scale;
- High accuracy and computational efficiency;
- A new way of extending a monocular visual odometry to its stereo version.

Our implementation [23] achieved a rate of over 60 frames per second (FPS) on a single CPU thread. We have evaluated DSVO in both real-world settings and in simulated environments inside the ROS Gazebo [20] simulator. When textures were clearly distinguishable, we demonstrated that DSVO works as well as, if not better than, state-of-the-art stereo-matching-based visual odometry in terms of accuracy and computational cost. In challenging scenarios where textures are repetitive and of high-frequency, state-of-the-art stereo-matching-based visual odometry failed, while DSVO continued to perform sufficiently well without significant degradation of accuracy or performance (see §4).

## 2 Related Work

The proposed approach builds on existing research in stereo and monocular visual odometry, some of which have already been discussed in the previous section. While stereo visual odometry has widely been explored, most [16, 26, 27] rely on stereo matching. S-PTAM [27] is one of the recent developments in stereo visual odometry, which extends PTAM [19] to stereo camera systems. It depends on stereo matching to generate new 3D points. Stereo ORB-SLAM [26] is another example of stereo visual odometry using stereo matching. Engel et al. extended their monocular LSD-SLAM [10] to stereo version in [11]. LSD-SLAM is purely based on direct method, but they adopted static stereo matching in the stereo version. However, stereo matching tends to fail for repetitive high-frequency textures, such as grass or sand. Wrong stereo correspondences lead to the wrong estimation of the 3D points which decrease the overall accuracy of visual odometry.

To decrease the chance of wrong stereo correspondences, some authors have looked at using global stereo matching for visual odometry. One such example is the visual odometry implemented by Stereolab for their ZED stereo camera. While the localization accuracy of this approach could be improved, real-time performance is achieved by performing stereo matching on a GPU. This results in higher power consumption which is undesirable for mobile robots.

On the other hand, Forster et al. extended their monocular SVO [13] using a different strategy rather than stereo matching. They extended monocular SVO for multi-camera systems, not particularly for a stereo camera, by tightly coupling all cameras to one error function. Computational cost is intensively increased because map-points are projected onto all camera frames. On the other hand, the explicit stereo configuration is not exploited.

# 3 Methodology

Figure 2 shows an overview of the DSVO algorithm. The notations used in the figure are listed below:

- $\mathbf{I}_i$: image frame from **Camera i**
- $R$: rotation estimated by Mono VO
- $\mathbf{R}$: optimized rotation
- $\underline{t}$: translation from Mono VO with unoptimized scale
- $\underline{\mathbf{t}}$: optimized translation with unoptimized scale
- $\mathbf{t}$: final translation
- $\mathbf{C}$: feature correspondences
- $\underline{\mathbf{X}}$: 3D map-points with unoptimized scale
- $\mathbf{X}$: final 3D map-points for new keyframe

DSVO is divided into two modules, driven by the functions of the two cameras in the stereo pair. **Camera 0** runs a monocular visual odometry (Mono VO) to track ego-motion $[R, \underline{t}]$. Mono VO also tracks new feature correspondences $\mathbf{C}$ temporally from frame to frame. When a new keyframe is selected, new 3D map-points are triangulated from the temporal feature correspondences $\mathbf{C}$. Then, bundle adjustment is performed to optimize motion $[\mathbf{R}, \underline{\mathbf{t}}]$ and structure (map-points) $\underline{\mathbf{X}}$ simultaneously. The results are

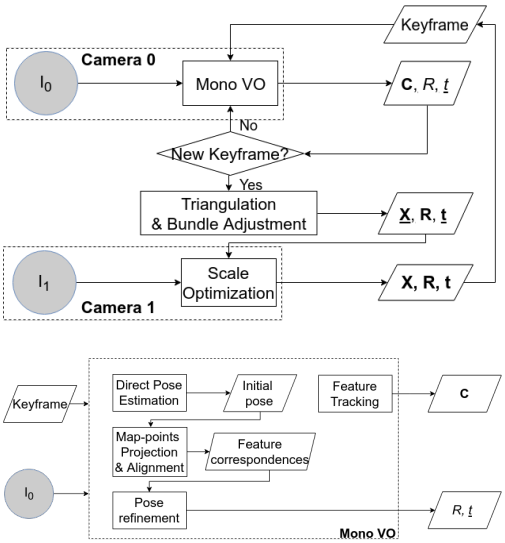


Figure 2: A flowchart showing the DSVO process. Cameras 0 and 1 form a stereo pair, with Camera 0 performing monocular VO and Camera 1 performing scale optimization.

handed over to **Camera 1** to optimize the scale. Eventually, the final structure $\mathbf{X}$ and motion $[\mathbf{R}, \mathbf{t}]$ are used to create a new keyframe for subsequent tracking.

The components of DSVO are explained in detail in the following subsections. The common notations are:

- $\mathbf{M_k}$: the set of map-points represented on frame k
- $\mathbf{W_X}$: the uncertainty of map-point $\mathbf{X}$
- $I_{\mathbf{X}}$: the pixel intensity of map-point $\mathbf{X}$
- $I_i(u, v)$: the pixel intensity of $I_i$ at location $(u, v)$
- $\mathbf{T}_i^j = [\mathbf{R}_i^j, t_i^j]$: transformation from frame i to frame j
- $\pi_i(\mathbf{T}, \mathbf{X}) = \mathbf{K}_i \cdot \mathbf{T} \cdot \mathbf{X}$: function projecting point $\mathbf{X}$ onto $\mathbf{I}_i$ by $\mathbf{T}$ and camera intrinsic parameter $\mathbf{K}_i$

## 3.1 Mono VO

Mono VO is a semi-direct visual odometry inspired by SVO [12]. The camera pose is initialized by minimizing the photometric error directly. Map-points are

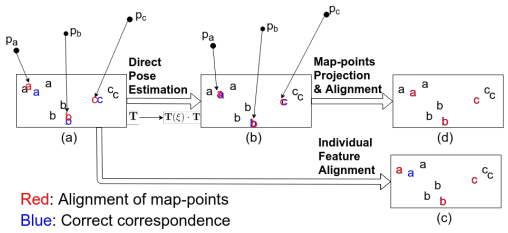


Figure 3: Mono VO design explanation. (a): original projection; (b): projection of Direct Pose Estimation; (d): final alignment; (c): alignment directly from (a), where **a** is mismatched.

then projected onto the current frame accordingly. Subsequently, the correspondence for each map-point is found individually without geometric constraint. Finally, the camera pose is refined by minimizing reprojection error.

The purpose of this two-step strategy is to ensure robustness in challenging scenes, particularly those of repetitive high-frequency textures. A simple example is illustrated in Figure 3. The direct method projects map-points onto the current frame according to its camera pose, as shown in Figure 3b, where the whole set of projections is controlled by a geometric model with only 6 degrees of freedom. Consequently, it is less likely to get wrong correspondences than individual alignment on the image, illustrated in Figure 3c. However, since map-points are not perfectly reconstructed, neither are the projections, but they should be close to the correct correspondences, as shown in Figure 3b. Aligning them individually from the projections is thus feasible. Based on the correspondences, the accuracy of the camera pose is further enhanced.

In addition to tracking the camera pose, Mono VO also tracks new feature correspondences $\mathbf{C}$. They will be used to reconstruct 3D map-points $\mathbf{X}$ for the next keyframe, so that Mono VO will not run out of map-points.

**Direct Pose Estimation** The goal in this step is to get an initial estimation $\mathbf{T}_{k-1}^{k}$ of the current camera pose with respect to the previous frame. It is accomplished by finding the projection with the minimum photometric error (intensity difference):

$$\mathbf{T}_{k-1}^{k} = arg\min_{\mathbf{T}} \frac{1}{2} \sum_{\mathbf{X}\in\mathbf{M_{k-1}}} e_0(\mathbf{T},\mathbf{X})^T \cdot \mathbf{W_X} \cdot e_0(\mathbf{T},\mathbf{X}) \tag{1}$$
$$e_0(\mathbf{T},\mathbf{X}) = I_{\mathbf{X}} - I_0(\pi_0(\mathbf{T},\mathbf{X}))$$

Each map-point $\mathbf{X} \in \mathbf{M_{k-1}}$ is brought to the current frame by $\mathbf{T}$. We mark the transformed point as $\mathbf{X}_c : [x, y, z]^T = \mathbf{T} \cdot \mathbf{X}$. Then it is projected onto the current image by $\pi_0$. The photometric error $e_0$ is the difference between the pixel intensity at the projection on $\mathbf{I_0}$ and the original intensity of $\mathbf{X}$. The error is weighted by map-point uncertainty $\mathbf{W_X}$.

Equation 1 is nonlinear in $\mathbf{T}$, and we use iterative Levenberg-Marquardt algorithm [25] to solve it. Since $\mathbf{T} \in SE(3)$, we use a twist $\xi \in se(3)$ to parameterize $\mathbf{T}(\xi) = exp(\xi)$, where $exp()$ is the exponential map. By the Chain Rule, the Jacobian of Equation 1 with respect to a perturbation $\xi$ is:

$$\mathbf{J}_{\xi} = \frac{\partial e_0(\mathbf{T},\mathbf{X})}{\partial \pi_0} \cdot \frac{\partial \pi_0(\mathbf{T}(\xi),\mathbf{X})}{\partial \mathbf{X}_c} \cdot \frac{\partial \mathbf{X}_c}{\partial \xi} \tag{2}$$

In each iteration, Equation 2 is used in Levenberg-Marquardt algorithm to solve for an updating twist $\xi$. Subsequently, $\mathbf{T}_{k-1}^{k}$ is updated accordingly. After the algorithm reaches convergence, we get an estimation of camera pose $\mathbf{T}_{k-1}^{k}$.

**Map-points Projection & Alignment** Since the map-points are not perfect, not all features are well aligned by the camera pose estimated in the previous step, illustrated in Figure 3b. Inspired by SVO, this step will align them further.

Even though the projections are not perfect, they should be close to the correct correspondences, illustrated in Figure 3b. Thus, Lucas-Kanade algorithm [2] is able to further align them correctly. In this step, each correspondence is found individually without geometric constraint. Eventually, we get the correspondences between map-points from the previous keyframe and pixels on the current frame: $\mathbf{M_{KF}} \leftrightarrow \{u_k\}$.

**Pose Refinement** Based on $\mathbf{M_{KF}} \leftrightarrow \{u_k\}$, the current pose is further refined. Iterative Levenberg-

Marquardt algorithm is used again to refine camera pose $\mathbf{T}_{KF}^k$ by minimizing the reprojection error:

$$\mathbf{T}_{KF}^k = arg\min_{\mathbf{T}} \frac{1}{2} \sum_{\mathbf{X} \in \mathbf{M_{KF}}} r_0(\mathbf{T}, \mathbf{X})^T \cdot \mathbf{W_X} \cdot r_0(\mathbf{T}, \mathbf{X}) \tag{3}$$

$$r_0(\mathbf{T}, \mathbf{X}) = u_k - \pi_0(\mathbf{T}, \mathbf{X})$$

where $\mathbf{T}$ is initialized as $\mathbf{T}_{k-1}^k \cdot \mathbf{T}_{KF}^{k-1}$.

After optimization, map-points with large reprojection error are removed from $\mathbf{M_{KF}}$ as outliers. In Figure 2, the optimized $\mathbf{T}_{KF}^k$ is marked as $[R, \underline{t}]$.

**Feature Tracking** As the camera moves farther away from the keyframe, fewer map-points are visible. Therefore, new points need to be inserted into the map to maintain tracking. We track features between consecutive frames using the Lucas-Kanade algorithm. Eventually, feature correspondences from the previous keyframe to the new keyframe are obtained, marked as $\mathbf{C}$ in Figure 2, and are used to construct new points for the new keyframe.

In scenes of repetitive high-frequency textures, such *temporal* stereo tends to be more accurate than *static* stereo, because feature correspondences between two keyframes are obtained with the help of many frames in between as intermediate bridges. With slow camera motion or high camera frame rate, the feature displacements between two consecutive frames are small. Hence, we are able to find the correspondence for each feature by searching within a small window around it. By contrast, for static stereo which has a relatively long baseline, feature displacements could be quite large. In scenes of repetitive high-frequency textures, it is very likely that there are several points along the epipolar line which are similar to the true correspondence, making it difficult to find the best match.

However, temporal stereo is sensitive to drastic camera rotation due to triangulation failure. When the proposed strategy fails, we call stereo matching to get 3D map-points, with the assumption that the texture of the scene is distinguishable for stereo matching.

## 3.2 Keyframe Selection

A new keyframe is selected when the distance between the current camera position and previous keyframe exceeds a certain threshold. To create a new keyframe, camera pose and map-points are needed. They are obtained by Triangulation & Bundle Adjustment, and Scale optimization described as follow.

## 3.3 Triangulation & Bundle Adjustment

From the Mono VO, we obtain the current camera pose $\mathbf{T}_{KF}^k = [R, \underline{t}]$, new feature correspondences $\mathbf{C} = \{u_{KF} \leftrightarrow u_k\}$, and map-points $\mathbf{X} \in \mathbf{M_{KF}}$ from the previous keyframe with the corresponding pixels $\{u_k\}$ on the current frame. We first triangulate the 3D points $\mathbf{X}$ from $\mathbf{C} = \{u_{KF} \leftrightarrow u_k\}$ and camera pose $\mathbf{T}_{KF}^k$. The results $\mathbf{X}$ and corresponding $u_k$ are concatenated into map-points $\mathbf{M_{KF}}$ and $\{u_k\}$. Next, camera pose and map-points are optimized together by Bundle Adjustment that minimizes the reprojection error:

$$[\mathbf{T}_{KF}^k, \mathbf{X}] = arg\min_{\mathbf{T},\mathbf{X}} \frac{1}{2} \sum_{\mathbf{X} \in \mathbf{M_{KF}}} [r_0^{KF}(\mathbf{X})^T \cdot \mathbf{W_X} \cdot r_0^{KF}(\mathbf{X}) + r_0^k(\mathbf{T}, \mathbf{X})^T \cdot \mathbf{W_X} \cdot r_0^k(\mathbf{T}, \mathbf{X})] \tag{4}$$

$$r_0^{KF}(\mathbf{X}) = u_X - \pi_0(\mathbf{I}, \mathbf{X}),\ r_0^k(\mathbf{T}, \mathbf{X}) = u_k - \pi_0(\mathbf{T}, \mathbf{X})$$

Where $u_X$ is the feature point on the previous keyframe associated with map-point $\mathbf{X}$.

The Iterative Levenberg-Marquardt algorithm is used to solve the above system. The optimized map-points and camera pose are marked as $\underline{\mathbf{X}}$, $[\mathbf{R}\ \underline{\mathbf{t}}]$ in Figure 2.

## 3.4 Scale Optimization

The map-points and camera pose optimized by Bundle Adjustment are not sufficient to create a new keyframe. Because everything described up to this point is essentially enables monocular visual odometry, the scale will drift.

The stereo baseline, which is the distance between the two cameras, is known from stereo calibration. The scale of monocular visual odometry can be aligned with the stereo baseline. The challenge is that there are no feature correspondences between the stereo frames. Instead, we optimize the scale by projecting the map-points from **Camera 0** to **Camera 1**, and minimizing the photometric error directly (hence the name *Direct* Stereo Visual Odometry):

$$s = arg\min_s \frac{1}{2} \sum_{\mathbf{X} \in \mathbf{M_{KF}}} e_1(s, \mathbf{X})^T \cdot \mathbf{W_X} \cdot e_1(s, \mathbf{X}) \quad (5)$$

$$e_1(s, \mathbf{X}) = I_{\mathbf{X}} - I_1(\pi_1(\mathbf{T}_{stereo},\, s \cdot \mathbf{X}))$$

For each map-point $\mathbf{X}$ with current scale s, we first bring it from **Camera 0** to **Camera 1** by $\mathbf{T}_{stereo}$, then project it to $\mathbf{I}_1$ by $\pi_1$. Subsequently, we compare the pixel intensity at the projection on $\mathbf{I}_1$ with the $\mathbf{X}$'s original pixel intensity.

Since the stereo frames are rectified, $\pi_1$ is simplified to

$$\begin{aligned} \pi_1(\mathbf{T}_{stereo}, s\mathbf{X})) &= \mathbf{K}_1 \cdot \mathbf{T}_{stereo} \cdot s\mathbf{X} \\ &= \begin{bmatrix} f & 0 & c_x \\ 0 & f & c_y \\ 0 & 0 & 1 \end{bmatrix} \cdot \begin{bmatrix} 1 & 0 & 0 & t_x \\ 0 & 1 & 0 & 0 \\ 0 & 0 & 1 & 0 \end{bmatrix} \cdot \begin{bmatrix} sx \\ sy \\ sz \\ 1 \end{bmatrix} \\ = \begin{bmatrix} fsx + c_x sz + ft_x \\ fsy + c_y sz \\ sz \end{bmatrix} &\doteq \begin{bmatrix} \frac{fx}{z} + c_x \\ \frac{fy}{z} + c_y \end{bmatrix} + \frac{1}{s} \cdot \begin{bmatrix} \frac{ft_x}{z} \\ 0 \end{bmatrix} \end{aligned}$$

Instead of optimizing $s$ directly, we optimize $\frac{1}{s}$ since $\pi_1$ is linear in $\frac{1}{s}$. The derivative of $\pi_1$ with respect to $\frac{1}{s}$ is

$$\frac{\partial \pi_1(\mathbf{T}_{stereo}, s\mathbf{X})}{\partial \frac{1}{s}} = \begin{bmatrix} \frac{ft_x}{z} \\ 0 \end{bmatrix}$$

which is a constant independent of $\frac{1}{s}$.

By Chain Rule, the Jacobian of Equation 5 with respect to $\frac{1}{s}$ is

$$\mathbf{J}_{\frac{1}{s}} = \frac{\partial e_1(\mathbf{T}, \mathbf{X})}{\partial \pi_1} \cdot \frac{\partial \pi_1(\mathbf{T}_{stereo}, s\mathbf{X})}{\partial \frac{1}{s}}$$

where $-\frac{\partial e_1(\mathbf{T}, \mathbf{X})}{\partial \pi_1}$ is the image gradient on $\mathbf{I}_1$.

The Iterative Levenberg-Marquardt algorithm is called again to solve this system. It is computationally efficient because $\frac{\partial e_1(\mathbf{T}, \mathbf{X})}{\partial \pi_1}$ can be pre-computed and $\frac{\partial \pi_1(\mathbf{T}_{stereo}, s\mathbf{X})}{\partial \frac{1}{s}}$ is constant for each point. On the other hand, the initial scale should not be far from the truth if Mono VO works properly. Quick convergence is expected.

Note that we match the entire set of features between stereo frames by optimizing *only* the scale parameter. Compared to explicit stereo matching, the proposed method thus is more robust to challenging scenes. Experimental evaluations described in the following section further underscore this point.

By adjusting the scale, the final map-points and translations are obtained, marked as $\mathbf{X}$ and $\mathbf{t}$ in Figure 2. Together with the rotation $\mathbf{R}$, a new keyframe is created for subsequent tracking in Mono VO.

# 4 Experimental Evaluation

We implemented DSVO on ROS [29] and OpenCV [6]. The Levenberg-Marquardt algorithm used for Equations (1), (3), (4), and (5) are performed by the g$^2$o [17] optimization framework. The computing platform was an ultrabook PC with a Intel$^{\text{TM}}$ Core i7-8550U CPU with 8 GB of RAM, and the DSVO implementation ran on a single thread.

We validated the accuracy, robustness, and efficiency of DSVO on three different datasets. We first showed that DSVO works as well as the state-of-the-art stereo visual odometry S-PTAM without the need for stereo matching. One of the datasets is from EuRoC [8], where textures are clear and distinguishable. We compared DSVO with S-PTAM in terms of accuracy and computational cost. The second dataset was simulated in the Gazebo simulator [20], where a scene of repetitive high-frequency textures was created. The goal was to show the robustness of DSVO over S-PTAM in challenging scenarios. Lastly, we ran DSVO on a dataset recorded by a ZED stereo camera in the real-world with challenging scenes.

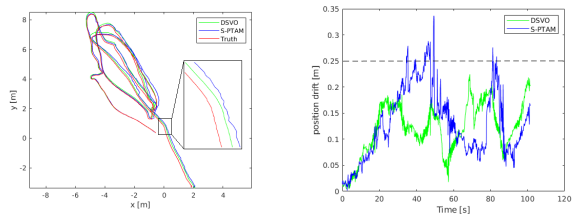


(a) Trajectories (top-view) (b) Absolute position error

Figure 4: Tests on MH_02 dataset

| Dataset | Method | Position [m/s] RMSE | Mean | Rotation[deg/s] RMSE | Mean | runtime[ms] Mean |
|---|---|---|---|---|---|---|
| MH_01 | DSVO | **0.0212** | **0.0101** | **5.3300** | **2.2819** | **27.873** |
| | S-PTAM | 0.0477 | 0.0158 | 8.1551 | 3.7272 | 61.915 |
| MH_02 | DSVO | **0.0203** | **0.0109** | **3.6068** | **1.3483** | **31.038** |
| | S-PTAM | 0.0259 | 0.0126 | 5.4878 | 2.7684 | 53.809 |
| MH_02 | DSVO* | 0.0299 | 0.0180 | 3.9414 | 1.909 | - |

Table 1: Comparison of relative position/rotation error per second and runtime per frame.

| Dataset | Mono VO Direct | Refine | Feat. Track. | Bun. Adj. | Scale Opti. | Ave. Time | Key-frame | # of points |
|---|---|---|---|---|---|---|---|---|
| MH_01 | 2.645 | 3.044 | 2.883 | 4.897 | 5.148 | **11.128** | 214 /2699 | 141.1 |
| MH_02 | 2.910 | 3.303 | 2.978 | 6.219 | 6.100 | **12.140** | 184 /2076 | 151.6 |

Table 2: Time taken (in milliseconds) by each sub-process of DSVO on MH datasets, at 5× of frame-rate to *stress-test* DSVO performance.

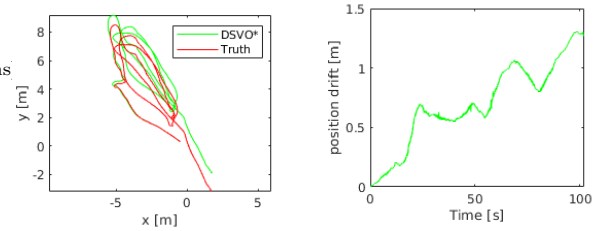


(a) Trajectories (b) Position drift

Figure 5: DSVO without scale optimization on MH_02 dataset.

## 4.1 EuRoC Dataset

We evaluated DSVO on the datasets MH_01_easy and MH_02_easy, which were recorded by a micro aerial vehicle (MAV) flying over a machine hall. The ground truth was measured by a Leica MS50 laser tracker. We ignored the first 50 seconds which are used to initialize the IMU since the IMU was not used in DSVO.

Figure 4a shows the comparison between the trajectories estimated by DSVO and S-PTAM on MH_02_easy dataset. Neither is far from the ground truth, given no loop closure was used in either DSVO or S-PTAM. However, DSVO generates a smoother trajectory than S-PTAM. In Figure 4b, the absolute position drift of DSVO never exceeds 0.25 meters, where the entire trajectory is roughly bounded by a $11.5m \times 7m \times 2.5m$ volume.

To test the accuracy of visual odometry, we report the relative position and rotation errors of the trajectories in Table 1. DSVO is slightly more accurate than S-PTAM on both datasets. On the other hand, the runtime of DSVO for each frame is almost half of that of S-PTAM. The runtime breakdown of DSVO at maximum performance is reported in Table 2. A rate of more than 60 frames per second is achieved, with over 140 map-points for each frame. Note that the current implementation of DSVO is single-threaded. However, in Mono VO, feature tracking can run in parallel with pose estimation, since they do not share any common data. Therefore, the runtime can be further reduced. Nevertheless, this evaluation shows that DSVO works as a means of stereo visual odometry, and it is computationally efficient.

Figure 5a shows the trajectory estimated by DSVO without scale optimization. The final position drift is increased from about 0.2 meter in Figure 4b to more than 1.2 meters in Figure 5b. The relative position and rotation error are also reported in Table 1 titled as DSVO*. They are higher than the errors of full DSVO, which demonstrates the effectiveness of the scale optimization process.

## 4.2 Gazebo Simulation

To evaluate DSVO in arbitrarily complex scenarios and have more control over the environment, we designed a custom world in Gazebo. It has a stereo

(a) A view of the mud world.

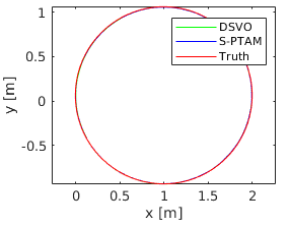


(b) Trajectories estimated in the mud world.

Figure 6: Gazebo 'mud world' simulation.

| Texture | Method | Position [m/s] RMSE | Mean | Rotation [deg/s] RMSE | Mean |
|---|---|---|---|---|---|
| Mud | DSVO | **0.0005** | **0.0003** | **0.3272** | **0.2736** |
| | S-PTAM | 0.0014 | 0.0009 | 0.6343 | 0.4697 |
| Grass | DSVO | **0.0014** | **0.0010** | **0.5665** | **0.4580** |
| | S-PTAM | failed | failed | failed | failed |

Table 3: Comparison of relative position/rotation error per second and runtime per frame.

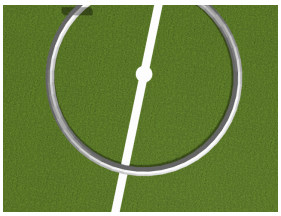

(a) View at the start position

(b) View after camera moves

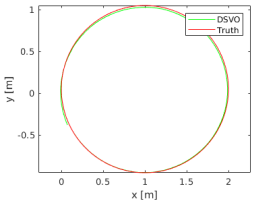


(c) Trajectory from DSVO

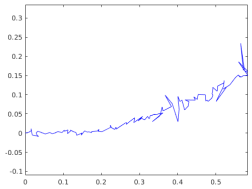

(d) S-PTAM failed

Figure 7: Gazebo 'grass world' simulation results for DSVO and S-PTAM.

camera 1 meter above and facing the ground. The stereo camera moves along a 1-meter-radius circle. The ground was rendered with different textures to test the robustness of DSVO.

First, we validated that the simulation setup was suitable for both DSVO and S-PTAM to work. We rendered the ground with the texture of Mud Box [14], illustrated in Figure 6a. Both DSVO and S-PTAM generates a trajectory of a circle in 1-meter radius, shown in Figure 6b. In Table 3, both algorithms have very small errors with mud texture.

To validate the robustness of DSVO over S-PTAM when the texture is repetitive with high-frequency, we replaced the mud texture with RoboCup 09 SPL Field [15], which we address as the 'grass world' as illustrated in Figure 7. Other than the texture, every other setting remains the same as in the mud world. In the beginning, the center line of the soccer field is visible, shown in Figure 7a, but as the camera moves away, nothing other than grass is visible, shown in Figure 7b. This absence of distinguishable features has been chosen on purpose to test the robustness of DSVO over S-PTAM.

As shown in Figure 7c, the trajectory estimated by DSVO is very close to the ground-truth. Furthermore, Table 3 shows that DSVO has a small error in this case. On the other hand, after the camera moved away from the center lines, not enough points from stereo matching were available for tracking, S-PTAM stopped tracking. Even with the center lines as distinguishable features, S-PTAM failed to closely match the actual camera trajectory, as Figure 7d shows.

## 4.3 Real-world Data

To validate the robustness of DSVO in outdoor settings, we used a ZED camera to record a stereo dataset, a snapshot of which is shown in Figure 8a. We carried the ZED camera by hand and walked an approximately $8m \times 8m$ square path with no elevation change. The camera was pointed at grass throughout. Since it was a sunny day, the brightness changed drastically when getting into the shadows.

Figure 8b shows the results. The trajectory estimated by DSVO is roughly a flat $8m \times 8m$ square, while S-PTAM generated a non-square trajectory and failed in the late stage. We also tested the perfor-

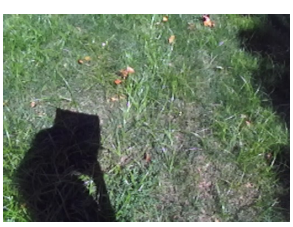

(a) A view of the dataset.

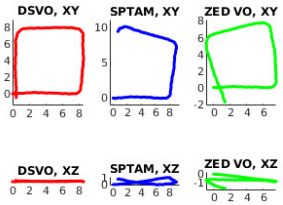


(b) Trajectories (in meters).

Figure 8: ZED camera experiment, ground-truth is approximately a zero-elevation, $8m \times 8m$ square.

mance of the visual odometry provided by the ZED camera SDK, which uses a GPU for better stereo matching. The result is shown in the right column of Figure 8b. As can be seen, the estimated trajectory is quite different from the actual $8m \times 8m$ square and also shows elevation change where there is none.

A video of DSVO accompanies the paper and is also available online [22], along with the datasets of §4.2 and §4.3 [24].

# 5 Conclusions

In this paper, we proposed a new algorithm for stereo visual odometry named DSVO that is independent of stereo matching. It combines the advantages of monocular visual odometry and stereo visual odometry. A semi-direct monocular visual odometry has been developed to track the ego-motion; meanwhile, the other camera in the stereo setup is used to optimize the scale of the monocular visual odometry. In experimental validations on simulated and real-world data, it has been shown to be accurate, fast, and robust in scenes of repetitive high-frequency textures. It also outperforms state-of-the-art stereo-matching-based visual odometry algorithms in these scenarios.

Future extensions to DSVO will include an IMU to form a stereo visual inertial odometry mechanism. An IMU would address the shortcomings in DSVO due to drastic rotation or visual degradation. Additionally, we are considering replacing Feature Tracking in §3.1 with probabilistic depth filter method [30] to achieve undelayed map-point initialization. We also intend to extend DSVO to a full SLAM algorithm including loop-closing abilities. The ultimate goal is to use DSVO on our autonomous underwater vehicle to enable accurate odometry and localization.

# Acknowledgment

The authors are thankful to Marc Ho and Julian Lagman for assistance with recording the datasets used for DSVO validation. We also gratefully acknowledge the support of the MnDrive initiative on this research.

## References


[1] P Aschwanden and W Guggenbuhl. Experimental results from a comparative study on correlation-type registration algorithms. *Robust computer vision*, pages 268–289, 1992.

[2] Simon Baker and Iain Matthews. Lucas-kanade 20 years on: A unifying framework. *International journal of computer vision*, 56(3):221–255, 2004.

[3] Dinkar N Bhat and Shree K Nayar. Ordinal measures for image correspondence. *IEEE Transactions on Pattern Analysis and Machine Intelligence*, 20(4):415–423, 1998.

[4] Frank Bignone, Olof Henricsson, Pascal Fua, and Markus Stricker. Automatic extraction of generic house roofs from high resolution aerial imagery. In *European Conference on Computer Vision*, pages 83–96. Springer, 1996.

[5] Michael Bloesch, Sammy Omari, Marco Hutter, and Roland Siegwart. Robust visual inertial odometry using a direct ekf-based approach. In *Intelligent Robots and Systems (IROS), 2015 IEEE/RSJ International Conference on*, pages 298–304. IEEE, 2015.

[6] Gary Bradski and Adrian Kaehler. Opencv. *Dr. Dobbs journal of software tools*, 2000.

[7] Myron Z Brown, Darius Burschka, and Gregory D Hager. Advances in computational stereo. *IEEE transactions on pattern analysis and machine intelligence*, 25(8):993–1008, 2003.

[8] Michael Burri, Janosch Nikolic, Pascal Gohl, Thomas Schneider, Joern Rehder, Sammy Omari, Markus W Achtelik, and Roland Siegwart. The euroc micro aerial vehicle datasets. *The International Journal of Robotics Research*, 35(10):1157–1163, 2016.

[9] Igor Cvišić and Ivan Petrović. Stereo odometry based on careful feature selection and tracking. In *Mobile Robots (ECMR), 2015 European Conference on*, pages 1–6. IEEE, 2015.

[10] Jakob Engel, Thomas Schöps, and Daniel Cremers. Lsd-slam: Large-scale direct monocular slam. In *European Conference on Computer Vision*, pages 834–849. Springer, 2014.

[11] Jakob Engel, Jörg Stückler, and Daniel Cremers. Large-scale direct slam with stereo cameras. In *Intelligent Robots and Systems (IROS), 2015 IEEE/RSJ International Conference on*, pages 1935–1942. IEEE, 2015.

[12] Christian Forster, Matia Pizzoli, and Davide Scaramuzza. SVO: Fast semi-direct monocular visual odometry. In *Robotics and Automation (ICRA), 2014 IEEE International Conference on*, pages 15–22. IEEE, 2014.

[13] Christian Forster, Zichao Zhang, Michael Gassner, Manuel Werlberger, and Davide Scaramuzza. Svo: Semidirect visual odometry for monocular and multicamera systems. *IEEE Transactions on Robotics*, 33(2):249–265, 2017.

[14] Gazebosim. Mud Box texture in Gazebo simulator. `http://models.gazebosim.org/mud_box/`. Online; accessed 14 September 2018.

[15] Gazebosim. RoboCup 09 SPL Field texture in Gazebo simulator. `http://models.gazebosim.org/robocup09_spl_field/`. Online; accessed 14 September 2018.

[16] Ruben Gomez-Ojeda and Javier Gonzalez-Jimenez. Robust stereo visual odometry through a probabilistic combination of points and line segments. In *Robotics and Automation (ICRA), 2016 IEEE International Conference on*, pages 2521–2526. IEEE, 2016.

[17] Giorgio Grisetti, Rainer Kümmerle, Hauke Strasdat, and Kurt Konolige. g2o: A general framework for (hyper) graph optimization. Technical report, Technical report, 2011.

[18] Andrew Howard. Real-time stereo visual odometry for autonomous ground vehicles. In *Intelligent Robots and Systems, 2008. IROS 2008. IEEE/RSJ International Conference on*, pages 3946–3952. IEEE, 2008.

[19] Georg Klein and David Murray. Parallel tracking and mapping for small ar workspaces. In *Mixed and Augmented Reality, 2007. ISMAR 2007. 6th IEEE and ACM International Symposium on*, pages 225–234. IEEE, 2007.

[20] Nathan P Koenig and Andrew Howard. Design and use paradigms for gazebo, an open-source multi-robot simulator. In *IROS*, volume 4, pages 2149–2154. Citeseer, 2004.

[21] Stefan Leutenegger, Simon Lynen, Michael Bosse, Roland Siegwart, and Paul Furgale. Keyframe-based visual–inertial odometry using nonlinear optimization. *The International Journal of Robotics Research*, 34(3):314–334, 2015.

[22] Jiawei Mo. DSVO Demonstration. `http://irvlab.cs.umn.edu/files/dsvomp4`. Online; accessed 14 September 2018.

[23] Jiawei Mo. DSVO Implementation. `https://github.com/jiawei-mo/dsvo`. Online; accessed 14 September 2018.

[24] Jiawei Mo. DSVO Test Datasets. `https://drive.google.com/open?id=14d7wK6QyGRZHCxDyhhjuaaSGoLBah7zz`. Online; accessed 14 September 2018.

[25] Jorge J Moré. The levenberg-marquardt algorithm: implementation and theory. In *Numerical analysis*, pages 105–116. Springer, 1978.

[26] Raul Mur-Artal and Juan D Tardós. ORB-SLAM2: An open-source slam system for monocular, stereo, and RGB-D cameras. *IEEE Transactions on Robotics*, 33(5):1255–1262, 2017.

[27] Taihú Pire, Thomas Fischer, Gastón Castro, Pablo De Cristóforis, Javier Civera, and Julio Jacobo Berlles. S-PTAM: Stereo parallel tracking and mapping. *Robotics and Autonomous Systems*, 93:27–42, 2017.

[28] Tong Qin, Peiliang Li, and Shaojie Shen. Vins-mono: A robust and versatile monocular visual-inertial state estimator. *IEEE Transactions on Robotics*, (99):1–17, 2018.

[29] Morgan Quigley, Josh Faust, Tully Foote, and Jeremy Leibs. Ros: an open-source robot operating system.

[30] George Vogiatzis and Carlos Hernández. Video-based, real-time multi-view stereo. *Image and Vision Computing*, 29(7):434–441, 2011.